JGR Oceans

RESEARCH ARTICLE
10.1029/2019JC015231

Variability and Trends of the Alaska Gyre From Argo and Satellite Altimetry

Hristina G. Hristova[1,2], **Carol Ladd**[2], **and Phyllis J. Stabeno**[2]

[1]Joint Institute for Marine and Atmospheric Research, University of Hawai'i at Mānoa, Honolulu, HI, USA, [2]NOAA/Pacific Marine Environmental Laboratory, Seattle, WA, USA

Key Points:
- Positive phase of PDO is associated with stronger and larger Alaska Gyre
- There is an increasing trend in strength of Alaska Gyre (but not areal extent) over 1993–2017
- Geostrophic advection plays a small role in interannual temperature/salinity variability in the Gulf of Alaska

Correspondence to:
H. G. Hristova,
hristina.hristova@noaa.gov

Citation:
Hristova, H. G., Ladd, C., & Stabeno, P. J. (2019). Variability and Trends of the Alaska Gyre from Argo and Satellite Altimetry. *Journal of Geophysical Research: Oceans*, *124*, 5870–5887. https://doi.org/10.1029/2019JC015231

Received 17 APR 2019
Accepted 23 JUL 2019
Accepted article online 1 AUG 2019
Published online 17 AUG 2019

Abstract The interannual variability and trends of the Alaska Gyre and Gulf of Alaska (GOA) circulation are examined using meridional geostrophic transport from Argo temperature and salinity (2004–2017) and altimetric sea surface height (1993–2017). More than half of the top 1,500 m meridional transport variability in the Alaska Gyre is accounted for by a statistical mode strongly correlated with the Pacific Decadal Oscillation (PDO) index, consistent with the PDO exerting a major influence on North Pacific sea surface temperature variability. During a positive phase of the PDO, the zero-transport streamline separating the subtropical from the Alaska Gyre is shifted to the south from its mean position, while more transport is diverted northward, associated with a stronger and larger Alaska Gyre. Additionally, over the 25-year altimetric record there is a linear, increasing trend in strength of the Alaska Gyre (but not in areal extent), accompanied by an increasing trend for the incoming North Pacific Current. The effect of the PDO transport mode on GOA circulation is weak. Temperature and salinity volume averaged for the GOA covary with the PDO index, with warmer and fresher waters during a positive phase. Despite correlated anomalies for temperature, salinity, and northward transport into the GOA, however, geostrophic advection from the south contributes only minimally to the interannual variations of water properties in the GOA. An exception was the marine heat wave of 2013/2014 and its aftermath when temperature advection from the south played a more appreciable role for warming and subsequent cooling of the GOA.

Plain Language Summary Variability of the ocean circulation in the Alaska Gyre is one of the factors influencing the rich ecosystem in the Gulf of Alaska. Improved understanding of the variability and trends of the Alaska Gyre is thus of prime concern, given its biologic and economic implications. Using data from the Global Argo program and satellite altimetry covering the 25-year period from 1993 to 2017, we diagnose the changes in Alaska Gyre structure and transport and how they fit in the larger picture of North Pacific global climate modes, such as the Pacific Decadal Oscillation (PDO). During a positive phase of the PDO, more transport is diverted northward, associated with a stronger and larger Alaska Gyre. Additionally, over the 25-year record the Alaska Gyre has continuously increased in strength (but not in size). While temperature and salinity in the Gulf of Alaska vary with the PDO, with warmer and fresher waters during a positive phase, advection from the south contributes only minimally to the year-to-year variations of water properties in the Gulf of Alaska, suggesting that these variations are mostly determined by local processes instead.

1. Introduction

In the northeast Pacific, the circulation is dominated by the broad eastward flowing North Pacific Current (NPC) and its bifurcation at the North American coast near 48°N (Figure 1). The bifurcation results in a southward flowing California Current and northward flowing Alaska Current, feeding the subtropical and Alaska Gyres, respectively (Chelton & Davis, 1982; Cummins & Freeland, 2007; Freeland, 2006). The Alaska Current morphs farther downstream near Kodiak Island into the Alaskan Stream, a narrow ~50-km intense western boundary current (Reed, 1984; Reed & Stabeno, 1989, 1993; Stabeno & Hristova, 2014). The continental shelf of the Gulf of Alaska (GOA) sustains a rich ecosystem despite downwelling favorable winds, promoted in part by various cross-shelf exchange mechanisms such as advection by eddies, flow in canyons, and downwelling relaxation due to episodic wind events (Ladd, Stabeno, et al., 2005, 2009; Mordy et al.,

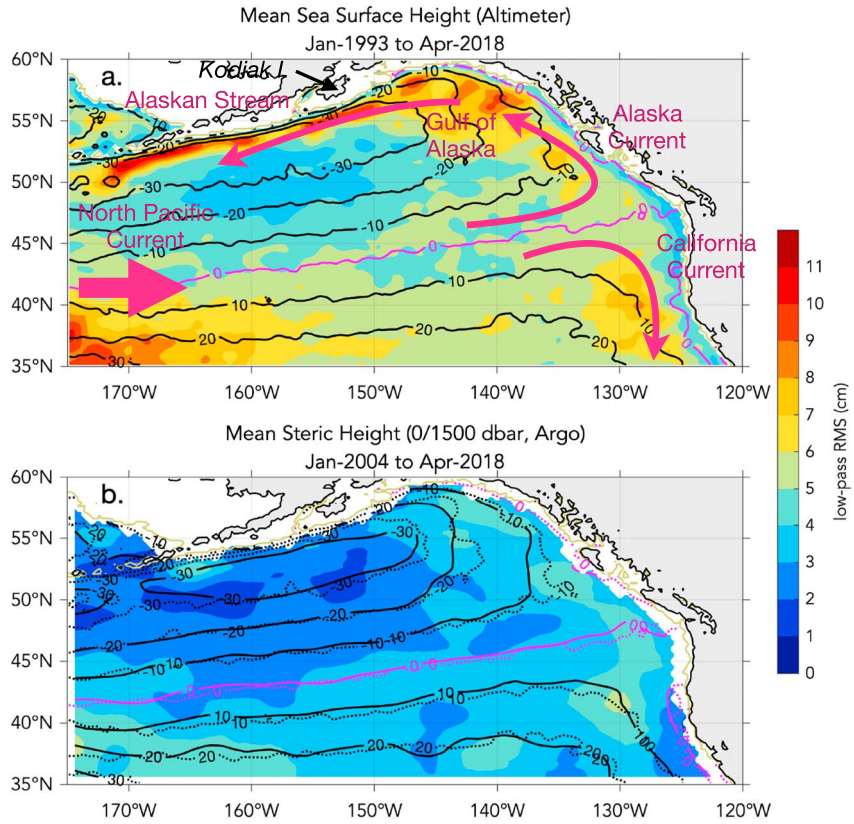

Figure 1. Time mean (black contours, centimeters) and RMS amplitude (shaded color, centimeters) of (a) sea surface height (SSH) from satellite altimetry (January 1993 to April 2018) and (b) steric height from Argo referenced to 1,500 dbar (January 2004 to April 2018). In (b), the SSH contours are overlaid in dotted lines for comparison. Altimetric data are masked for depths shallower than 200 m (isobath shown in gold). Both SSH and steric height are shifted by a constant—the value of the SSH or steric height contour separating the subtropical from the Alaska Gyre. As a result, for both variables the bifurcation contour is the zero-height contour, shown in purple. RMS = root-mean-square.

2019; Stabeno et al., 2004) that result in the exchange of iron and micronutrients between the shelf and the basin and affect larval transport.

Oceanic variability in the northeast Pacific is routinely discussed in terms of global climate modes: the Pacific Decadal Oscillation (PDO; Mantua et al., 1997) and the North Pacific Gyre Oscillation (NPGO; Di Lorenzo et al., 2008). Both of these modes describe covariability between atmospheric forcing patterns, ocean circulation, upper ocean temperature, and primary production in the coastal regions (e.g., Hermann et al., 2016; Di Lorenzo et al., 2013). While ocean modes of variability are often examined using sea surface temperature (SST), sea surface height (SSH), which represents the integrated influence of temperature and salinity anomalies through the water column, is also a robust indicator of the climate state of the upper ocean (Cummins et al., 2005). Because of its biological and economic implications, improved understanding of the variability and trends of the GOA circulation and its place in the larger picture of global climate modes is of prime concern.

Previous studies suggest that on seasonal and longer time scales, variability in the GOA occurs mostly as residuals in the alongshore currents around the boundaries of the basin (Chelton & Davis, 1982; Strub & James, 2002a, 2002b). Model experiments indicate that local wind forcing is the primary driver for the low-frequency circulation variability in the northeast Pacific (Cummins & Freeland, 2007; Cummins & Lagerloef, 2004), with signals propagating along the coast from the tropics contributing as well (Qiu, 2002). Douglass et al. (2006) and Cummins and Freeland (2007) identified two separate modes of transport variability involving the NPC and its bifurcation at the coast, consisting of either compensating or correlated anomalies of the California and Alaska Currents. SSH differences across the NPC are often used to study the split of transport at its bifurcation and correlate strongly with variations in the transport stream

function evaluated from numerical models (Cummins & Freeland, 2007). Analysis of isopycnal depth variations in the GOA shows that the PDO influences the water column through, at least, the top 1 km (Cummins & Masson, 2018). On interannual time scales, the depth of the main pycnocline undergoes variations consistent with a low-frequency modulation of the Alaska Gyre circulation, intensified during the warm phase of the PDO. The role of advection from the west for the development of temperature anomalies in the GOA is not, however, clearly established (Cummins & Masson, 2018; Freeland, 2002).

In this study we rely on two complementary global data sets (Argo temperature and salinity, and satellite altimetry) to examine the variability of the GOA circulation over the last 25 years (1993–2017). While part of this data set has been examined before, the length of the available record, spanning two and half decades, allows to better establish any long-term trends in the circulation. Using the meridional transport stream function, we diagnose the changes in Alaska Gyre structure and transport and how they fit in the larger picture of North Pacific global modes of variability. We also aim to quantify the implications of transport variability at the NPC bifurcation for temperature and salinity variability in the GOA.

This article is organized as follows. Section 2 describes the observational data sets and methods used in this study. Section 3 presents the transport variability and trends for the northeast Pacific in general, while section 4 focuses on the implications for the GOA and Alaska Gyre circulation. Summary and conclusions are given in section 5.

2. Data

2.1. Gridded Temperature and Salinity From Argo

The vertical structure of temperature and salinity for the northeast Pacific was obtained from the Roemmich-Gilson Argo Climatology (http://sio-argo.ucsd.edu/RG_Climatology.html; Argo, 2000; Roemmich & Gilson, 2009). The data set provides global, monthly, 1° latitude by 1° longitude gridded temperature and salinity on 58 vertical pressure levels extending from surface to 2,000 dbar and covers the period from January 2004 to April 2018 (14.33 years).

Argo temperature and salinity were used to calculate steric height and geostrophic shear for the top 1,500 m of the water column, according to TEOS-2010 (IOC et al., 2010; McDougall & Barker, 2011). Steric height is defined as the vertical integral from surface to a given pressure level of the specific volume anomaly, $\delta(T, S, p)$, divided by the gravitational acceleration, g. For the results presented here, $\delta(T, S, p)$ was integrated to 1,500 dbar, which we show is sufficient to capture the bulk of the GOA baroclinic signal associated with the slope of the steric height at surface (section 3.1). Geostrophic shear referenced to 1,500 dbar was also computed and used to determine the 0- to 1,500-m meridional transport (section 3.3), as well as a vertical section of northward velocity into GOA at 50°N (section 4.4).

2.2. Sea Surface Height From Altimetry

Altimetric SSH provides a decade longer record of surface variability for the northeast Pacific. SSH was obtained from the multisatellite merged gridded sea level anomalies produced and distributed by the Copernicus Marine and Environmental Monitoring Service (http://marine.copernicus.eu), to which we added a mean dynamic ocean topography (Maximenko et al., 2009). The result is the absolute ocean dynamic topography, the derivatives of which provide the absolute surface geostrophic velocity. Sea level anomalies are available as daily maps on a $\frac{1}{4}°$ grid and cover the period from January 1993 to April 2018 (25.33 years). The last year of data used here (since May 2017) consist of near-real-time data, so their processing is only preliminary and the fields are noisier. The (Maximenko et al., 2009) mean dynamic topography is based on surface drifter velocities and satellite measurements and is thus independent of the in situ Argo data.

Prior to analysis, SSH was low-pass filtered to better match the time scales resolved by the monthly Argo data as follows. We first determined a 12-month annual cycle by calculating monthly averages over the 25.33-year record. The residual from the annual cycle was then smoothed with a 91-day running mean, applied twice (half-power at 205 days, ~7 months), shortening the time series by 3 months at both ends. All altimetric analyses performed here are based on the low-pass filtered SSH, consisting of the sum of the annual cycle and low-frequency (smoothed) residual. The altimetric surface geostrophic velocity was also computed based on the low-pass filtered SSH by centered differences. SSH and associated velocities for ocean depths shallower than 200 m were masked.

To compare altimetric and Argo time series to each other or to various climate indices, we compute the correlation coefficient r and its p value, using a two-tailed Student's t test of r being significantly different from 0 (the null hypothesis). Based on autocorrelations, we assume 18 degrees of freedom for all altimetric series, and 12 degrees of freedom for all Argo series, that is, slightly less than the total number of years of available data, allowing for some autocorrelation between the years. We report the p values rounded to the commonly used 10%, 5%, and 1% significance levels. For example, $p < 0.05$ means that there is less than 5% probability that we would obtain as large (or larger) correlation r if the two time series were uncorrelated.

3. Comparison of Steric Height and SSH for the Northeast Pacific

3.1. Reference Level for Steric Height

In the northeast Pacific, defined here as the region east of 175°W and north of 35°N, the circulation is dominated by the NPC and its bifurcation (Figure 1). Both steric height from Argo temperature and salinity and SSH from satellite altimetry (when a mean dynamic topography is included) provide streamlines of surface geostrophic flow.

Our focus through this paper is primarily on the northward branch and GOA circulation that includes the Alaska Current, Alaskan Stream, and cyclonic Alaska Gyre. In the time mean, one can easily identify a bifurcation streamline—a contour of SSH or steric height that separates the Alaska Gyre from the subtropical gyre (Figure 1; purple contours). To facilitate the comparison between steric height and SSH slopes, we have shifted both fields by a constant value (55 cm for SSH and 169 cm for steric height referenced to 1,500 dbar), so that the bifurcation streamline (for the mean over the respective data period) corresponds to the zero contour.

The nearly overlapping contours of mean steric height and SSH indicate that density variations above 1,500 dbar account for the bulk of the baroclinic structure seen at the surface, at least away from the slope (Figure 1b). The Alaska Gyre with its cyclonic circulation corresponds to a depression of surface height. The minimum of steric height in the Alaska Gyre (−35 cm) is within 12% of the SSH minimum (−39.4 cm). The subtropical gyre, only a small part of which is included in the region analyzed here, corresponds to a positive surface height, with a maximum located in the southwest corner of our region. For comparison, steric height referenced to a shallower pressure level of 1,000 dbar misses about 20% of the Alaska Gyre signal and 5% of the subtropical gyre signal. Thus, subthermocline density variations matter, especially in the interior Alaska Gyre. In what follows, steric height is referenced to 1,500 dbar; a deeper reference level (2,000 dbar) does not add significantly to the surface signal, while it limits the calculation to regions where ocean depth is at least 2,000 m.

3.2. Surface Variability and Trends

The spatial pattern of surface variability in the northeast Pacific is similar in both steric height and altimetry, although the picture is somewhat diluted in the Argo steric height field (Figure 1). Maxima in root-mean-square (RMS) SSH and steric height are located offshore in the California Current System, along the path of the Alaskan Stream (mostly in altimetry), and in the eastern GOA where the circulation is dominated by large eddies (Crawford, 2002; Ladd, Kachel, et al., 2005; Tabata, 1982). The enhanced variability in the subtropical gyre near the dateline south of 40°N is a manifestation of the Kuroshio Extension (e.g., Qiu et al., 2007).

Despite the similarity in spatial pattern, the RMS magnitude of SSH is larger than that of steric height by a factor of 2 in the basin interior, and by even more around the boundary of the basin (Figure 1). The discrepancy in magnitude is due in part to differences in sampling and resolution, especially near the coast where boundary currents and eddy variability are poorly resolved in the 1° monthly Argo product. More fundamentally, however, the steric effect—the expansion or contraction of a water column due to changes in its heat or salt content—is only one of the factors contributing to SSH variability. Deep steric height variability (below 1,500 dbar), as well as nonsteric processes (direct changes in total ocean mass and water mass redistribution in the oceans) are potential contributors too.

Spatial average over the northeast Pacific further quantifies the differences in RMS magnitude of SSH and steric height. Both SSH and steric height, when averaged over the region, exhibit a clear annual cycle and a long-term trend, significant at 90% confidence level (Figure 2b). The annual cycle amplitude of SSH matches closely that of steric height. This is expected given that seasonal changes in SSH in the subpolar gyre are mostly due to temperature variability above the thermocline and thus should be accounted for by

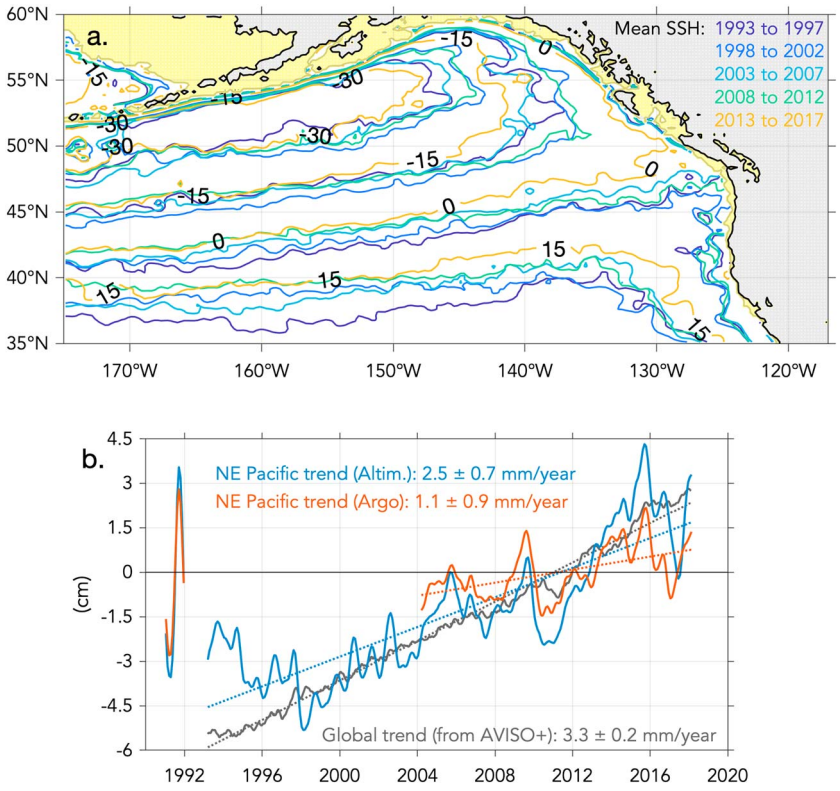

Figure 2. (a) SSH (contour interval 5 cm) averaged in 5-year increments showing a rising trend over the northeast Pacific that is not spatially uniform. (b) Spatially averaged over the northeast Pacific SSH (blue line) and steric height from Argo (red line) compared to the global mean sea level rise from AVISO+ (black line). For all three curves, the time mean over the Argo period (2004–2017) and annual cycle are subtracted prior to computing a linear trend (trend shown in matching color dotted line), with its uncertainty (90% confidence interval) indicated in the legend. The annual cycle for SSH (blue line) and steric height (red line) is plotted at left starting in January 1991. SSH = sea surface height.

steric height referenced to 1,500 dbar (e.g., Vivier et al., 1999). By contrast, the linear trend in steric height (1.1 ± 0.9 mm/year for 2004–2017 and the region considered here) is about one third of the SSH trend when computed for the same period (3.3 ± 1.5 mm/year for 2004–2017 and the region considered here). This falls in line with ocean warming contributing roughly 30% to the global sea level budget for the past two decades (Cazenave & Remy, 2011; Cazenave et al., 2018). Over the longer altimetric record, the linear trend in SSH (2.5 ± 0.7 mm/year for 1993–2017 and the region considered here) is less than the global rate of sea level rise (3.3 ± 0.2 mm/year; mean sea level from AVISO+, https://www.aviso.altimetry.fr). Accumulated over the 25-year altimetric record, the trend in SSH for the northeast Pacific adds up to a rise of 6.25 cm since 1993, comparable to the 7-cm peak-to-peak amplitude of its annual cycle.

The trend in SSH over the northeast Pacific is not spatially uniform; nor is it stationary, as illustrated by 5-year averages of SSH (Figure 2a). Over the altimetric period, there is a consistent rise in SSH over the subtropical gyre, with the largest changes observed in the south. The bifurcation streamline, identified as the zero contour of SSH, where SSH has been referenced to the same constant value, 55 cm, based on the full record time mean (see section 3.1), has also shifted northward, at an approximately constant rate since 1993. However, there is no clear trend in the interior Alaska Gyre. The gyre is most contracted in the earliest (1993–1997) and latest (2013–2017) pentads and more expanded in the middle of the record (especially 1998–2002 and 2008–2012), as measured by the location of the −15- and −30-cm SSH contours (Figure 2a).

The spatially nonuniform variations in SSH, and in particular the SSH difference across the bifurcation streamline, imply long-term changes in the NPC, while the northward movement of the bifurcation streamline is suggestive of variability in the strength and areal extent of the Alaska Gyre. Some caution is warranted, however: A constant value of SSH may not be the best descriptor of the boundary between the subtropical and Alaska Gyres over decades spanning record. Indeed, early in the record the zero SSH contour turns south along the North American coast, while later in the record, it turns north (Figure 2a). It is possible

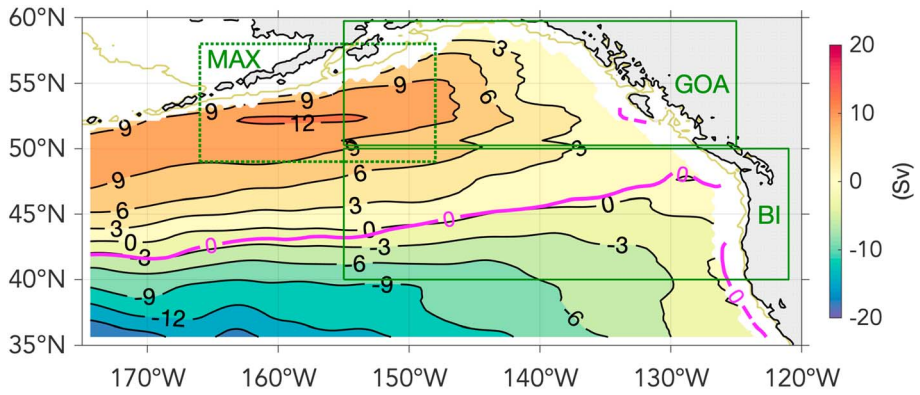

Figure 3. Mean meridional geostrophic transport for the top 1,500 m based on Argo geostrophic velocity, integrated zonally (starting from 0 at the eastern boundary). Overlaid in magenta for reference is the zero contour of mean steric height, separating the subtropical from the Alaska Gyre. The green rectangles mark three regions of interest: the region (MAX) of maximum Alaska Gyre transport (see section 4.2), the bifurcation (BI) region (see section 4.3), and the Gulf of Alaska (GOA) region (see section 4.4).

that the bifurcation occurs at a slightly different SSH over time (due, e.g., to sea level rise). A velocity-based quantity may thus be better suited to describe the bifurcation variability and gyre size changes on decadal time scales and is addressed in the next section.

3.3. Meridional Geostrophic Transport From Argo and Altimetry

We define the meridional geostrophic transport Ψ^{1500} (units of Sverdrup, 1 Sv = 10^6 m^3/s) as the vertically integrated to 1,500-m meridional geostrophic velocity from Argo, integrated zonally east to west, starting from the North American coast. The time mean meridional geostrophic transport is similar in pattern to the time mean steric height (Figure 3 vs. Figure 1). North of the bifurcation streamline, Ψ^{1500} is positive indicating cyclonic flow in the Alaska Gyre, while south of the bifurcation, Ψ^{1500} is negative indicating anticyclonic flow in the subtropical gyre. The transport of the Alaskan Stream is not properly resolved in this calculation, the 1° resolution of the gridded Argo data being too coarse for this narrow (∼ 50 km; Stabeno & Hristova, 2014) western boundary current.

It can be shown that Ψ^{1500} is the depth-integrated to 1,500-m steric height, $H(x, y)$, scaled by the local value of $-g/f$, and with the value on the eastern boundary subtracted away, that is, $\Psi^{1500} = -\frac{g}{f}\left(H(x,y) - H(x_E,y)\right)$ where x_E is the longitudinal location of the eastern boundary. Since there are generally no strong geostrophic flows into or out of the eastern boundary region, $H(x_E, y)$ is expected to vary only weakly with latitude. As a result, Ψ^{1500} is effectively a scaled version of H and, as such, can be considered an approximate stream function for the geostrophic transport, $(U, V) \simeq \left(\Psi^{1500}_y, -\Psi^{1500}_x\right)$, relative to no motion level of 1,500 m. The field shown in Figure 3 is therefore a scaled version of the depth-integrated steric height given in Figure 2 of Cummins and Masson (2018), where it can be verified that $H(x_E, y)$ is indeed nearly constant.

As a next step, we rely on the Argo data set to "translate" the longer (and more detailed) altimetric SSH record and its associated surface geostrophic velocity into meridional transport stream function, Ψ^{1500*}, representative of the transport over the top 1,500 m of the water column. Experimentation with the Argo data set shows that in the northeast Pacific, Ψ^{1500} can be reasonably well approximated by linear interpolation from the *surface* meridional geostrophic transport (i.e., the east-to-west integral of surface meridional geostrophic velocity from Argo steric height). Using this as justification, we start by computing Ψ^0, the zonal east-to-west integral of the surface meridional geostrophic velocity from altimetry (units of square meters per second). We then transform Ψ^0 into 0- to 1,500-m transport (units of Sverdrup) using a linear relationship,

$$\Psi^{1500*} = P_0(x)\Psi^0 + P_1(x), \tag{1}$$

where the coefficients $P_0(x)$ and $P_1(x)$ are obtained by least squares fit between Ψ^0 (from altimetry) and Ψ^{1500} (from Argo). The least squares fit is calculated separately for each longitude and using the time mean Ψ^0 and Ψ^{1500} for the overlapping 2004–2017 period. With this definition, the meridional transport computed from altimetry is in effect proportional to the SSH difference between the coast and a given location multiplied by a depth scale, P_1 (increasing away from the coast from 100 to 400 m) and shifted by a value P_0 (between 0 and 2 Sv, also increasing away from the coast).

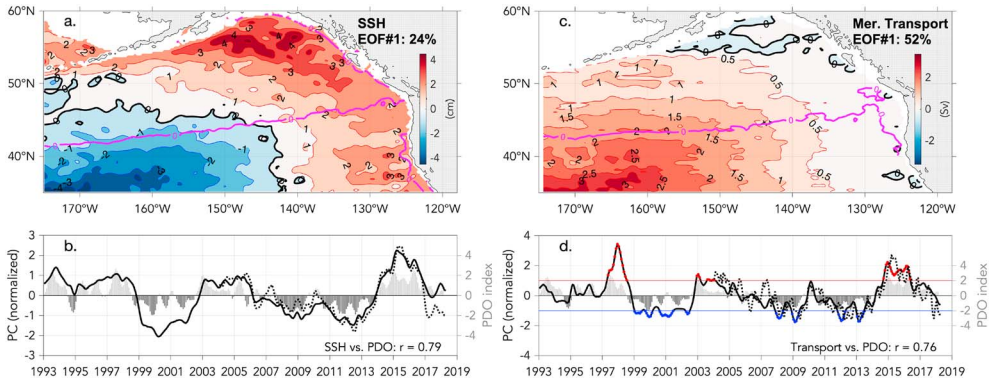

Figure 4. Leading EOF and its principal component for (a, b) SSH and (c, d) meridional geostrophic transport from altimetry (see section 3.3 for definition). (a and c) The spatial structure of the EOF, with the percentage of explained variance marked on each plot. Overlaid in purple is the contour separating the subtropical from the Alaska Gyre. (b and d) The principal component for each EOF (solid black line), normalized by the standard deviation. Overlaid in dotted lines are the principal components for the leading EOF using Argo data instead: steric height for (b), and 0- to 1,500-m meridional transport for (d). The PDO index is shown in gray shading (axis on the right); its correlation with the principal component is marked on each plot. In (d) only, the months corresponding to positive/negative phase of the leading EOF (when the principal component exceeds ±1 standard deviation) are highlighted in red/blue, respectively. EOF = empirical orthogonal function; SSH = sea surface height; PDO = Pacific Decadal Oscillation; PC = principal component.

By construction, the magnitude of the time mean meridional transport estimated from altimetry (not shown here) closely matches the actual transport above 1,500 m computed from Argo (Figure 3). As we will see next, although the mean meridional transport from altimetry looks similar to the mean SSH, the spatial pattern of variability is different (since Ψ^{1500*} implies changes in transport, i.e., SSH gradient).

3.4. Statistical Modes of Transport Variability

We use empirical orthogonal function (EOF) analysis to examine and compare variability in SSH and meridional transport for the northeast Pacific. The first EOF of SSH variability (where the seasonal cycle and a linear trend are removed at each grid point) accounts for 26% of the surface variability for the period 1993–2017 (Figures 4a and 4b). Consistent with previous studies (e.g., Cummins et al., 2005; Di Lorenzo et al., 2008), this mode captures the signature of the PDO in the northeast Pacific. Its spatial pattern has a dipole structure with in-phase variations of SSH in a broad band along the coast from California to GOA, and opposite sign SSH anomaly in the interior of the basin. Its principal component is strongly correlated with the PDO index ($r = 0.79$, $p < 0.01$; PDO index from http://research.jisao.washington.edu/pdo). EOF analysis of steric height from Argo results in a leading mode with similar spatial and temporal structure, explaining a slightly larger percentage of variance (39% for the period 2004–2017). Only the principal component for the Argo mode (normalized by its standard deviation) is shown in Figure 4b and matches closely the altimetric one.

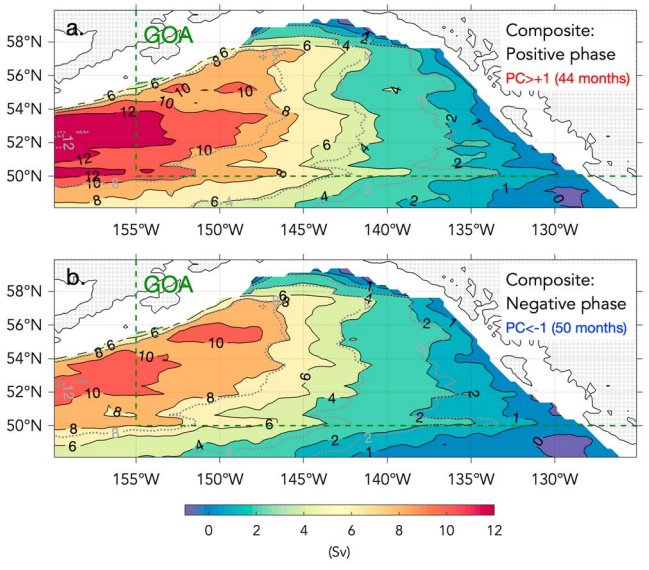

Figure 5. Composites of meridional geostrophic transport from altimetry for the GOA region corresponding to (a) positive, and (b) negative phase of the leading EOF. The composites represent time average over the months when the principal component of the EOF exceeds ±1 standard deviation (see Figure 4d). For reference, selected time mean transport contours for the full data period (2, 4, 8, and 12 Sv) are shown in gray dotted lines. The green rectangle refers to the GOA region (same as in Figure 3; see section 4.4). GOA = Gulf of Alaska; EOF = empirical orthogonal function.

Previous studies have identified a second statistical mode of SSH variability of importance in the North Pacific, the NPGO, representing in-phase variations of the subtropical and Alaska Gyres (Di Lorenzo et al., 2008). For the period and data considered here, a mode with NPGO-like spatial structure appears as mode 2 in the EOF analysis. It accounts for 9% of the SSH variability; however, the mode is not statistically significant (and is not shown). The absence of the NPGO mode for the data examined here is to be expected: over the altimetric period 1993–2017, the PDO and NPGO indices are negatively correlated ($r = -0.75$, $p < 0.01$; NPGO index from http://www.o3d.org/npgo). Thus, it is not surprising that EOF

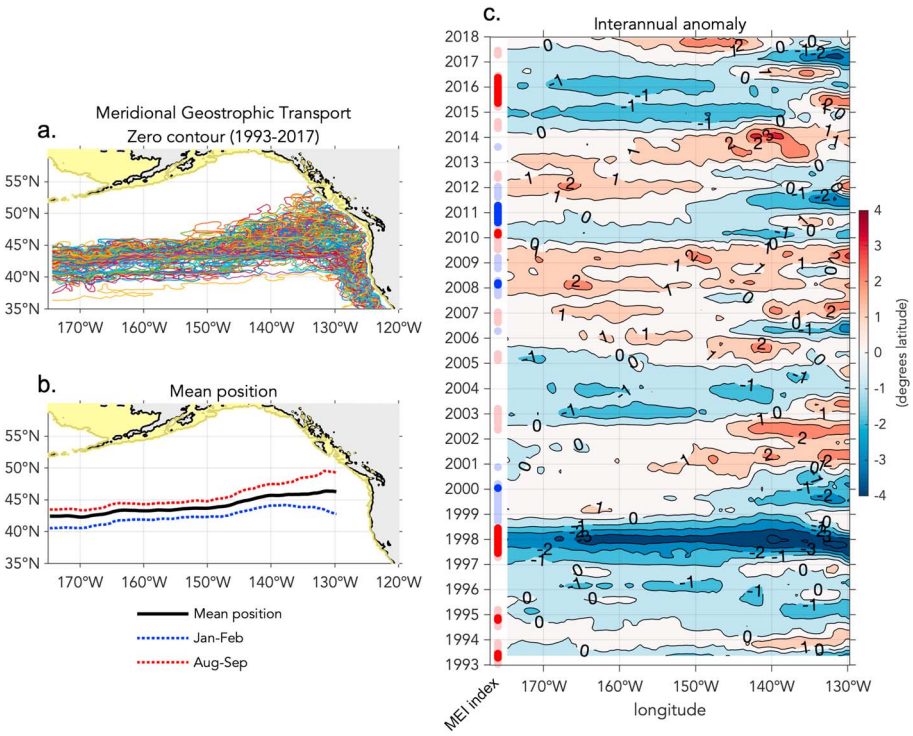

Figure 6. Variability of the position of the zero meridional transport contour, separating the subtropical from the Alaska Gyre. Shown are (a) all zero contours, overlaid, for the period 1993–2017, (b) the mean position of the zero contour and its seasonal deviations, and (c) the low-pass filtered (>7 months) interannual variability of the zero contour as a Hovmöller diagram of longitude versus time. Northward deviation (red shading) indicates smaller Alaska Gyre; southward deviation (blue shading) indicates larger Alaska Gyre. Shown along the time axis is the Multivariate ENSO Index (MEI) with dark (light) red indicating strong (moderate) El Niño conditions, and dark (light) blue, strong (moderate) La Niña conditions.

analysis consisting of projecting a field's variance onto mutually orthogonal eigenmodes is unable to isolate the NPGO mode of surface variability.

EOF analysis of meridional geostrophic transport as estimated from altimetry shows a much larger fraction of the variance (52% for the period 1993–2017) explained by its first statistical mode (Figures 4c and 4d). Much like for SSH, the principal component for the transport mode is strongly correlated with the PDO index ($r = 0.76$, $p < 0.01$). Its amplitude is positive over the entire northeast Pacific region considered here, with the exception of the GOA. Thus, in a positive phase the Alaska Gyre is stronger, while the subtropical gyre is weaker, accompanied by a southward shift of the zero-transport contour separating the Alaska Gyre from the subtropical gyre to the south. In the GOA, and especially to the northeast, the EOF amplitude is weak to slightly negative, implying that although in a positive phase the large-scale Alaska Gyre is stronger, the circulation in the local GOA is only weakly modified (Figure 5). The slightly negative values in the head of the GOA are suggestive of a broadening and/or offshore shift of the Alaska Current and Alaskan Stream. These near-shelf values for the meridional transport should, however, be considered with caution since they are sensitive to the limited near-costal spatial coverage of the data sets used here. Nevertheless, the overall implications of a stronger Alaska Gyre and weak modal amplitude in the eastern GOA (as compared to the western GOA) during a positive phase of the PDO are consistent with model-based multivariate analysis (Hermann et al., 2016).

The amplitude of the leading transport EOF is largest in the subtropical gyre, bringing the possibility that it may not be as representative for the Alaska Gyre. EOF analysis performed on the meridional geostrophic transport north of 45°N identifies, however, a nearly identical first mode, including the weakly negative amplitude in the eastern GOA. The variability of meridional transport described by its leading EOF (Figures 4c and 4d) is consistent with the transport variability expected from the SSH leading mode

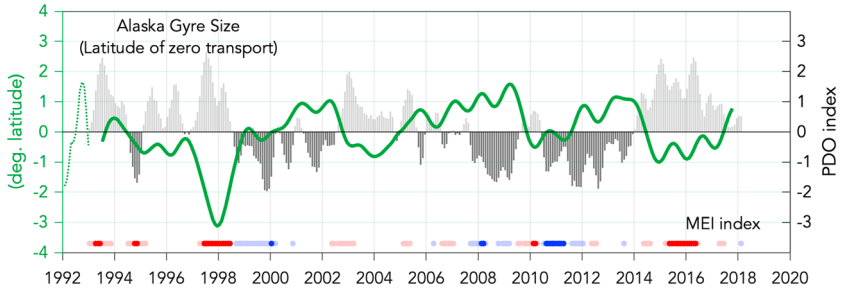

Figure 7. Interannual variability of Alaska Gyre size (green line), as described by the zonal average of the interannual deviations of the zero meridional transport contour from its mean position (Figure 6c). Southward deviation (negative value) means larger Alaska Gyre, while northward deviation (positive value) means smaller Alaska Gyre. The annual cycle of Alaska Gyre size is plotted once starting in January 1992 (green dotted line). Shaded in gray is the PDO index (axis on the right). The MEI is plotted along the time axis, with dark (light) red indicating strong (moderate) El Niño, and dark (light) blue, strong (moderate) La Niña conditions. PDO = Pacific Decadal Oscillation; MEI = Multivariate ENSO Index .

(Figures 4a and 4b). Directly analyzing the transport shows that PDO-like variability accounts for a larger fraction of the low-frequency variance in the northeast Pacific than suggested by SSH.

4. Implications for the GOA Circulation

In this section we focus in more detail on the Alaska Gyre and GOA circulation. We are interested in quantifying the interannual variability and trends in gyre areal extent (section 4.1), gyre strength (section 4.2), split of transport at the bifurcation latitude (section 4.3), and advective contribution by the geostrophic flow to the changes in heat and salt content in the GOA (section 4.4).

4.1. Size of the Alaska Gyre: Bifurcation Latitude

The zero meridional transport contour marks the separation between northward and southward flow and serves as the boundary between the subtropical and Alaska Gyres (Figure 3). We can thus use the meridional transport to determine the interannual variability and any long-term trends in the areal extent (or size) of the Alaska Gyre by tracking through time the position of the zero-transport contour. We first collect the set of zero-transport contours from the SSH-estimated meridional transport for the 25-year long altimetric record (Figure 6a). These contours are then mapped on a uniformly spaced longitude axis, covering the range 175–130°W with a 0.5° longitude resolution, averaging out in the process small spatial scale deviations. We do not attempt to map the zero-transport contours all the way to the coast since the bifurcation is not well defined there in the daily maps; the near-coastal variations (although typically large) do not signify changes in the Alaska Gyre structure. In the instantaneous fields, the position of the zero-transport contour can vary significantly. For example, at 175°W, the western most edge of the region considered here, the mean bifurcation latitude is 42.5°N, but varies between 37°N to 45°N (Figure 6a).

Part of the zero-transport latitude variability is accounted for by seasonal changes. These are largest near the coast: The bifurcation latitude shifts north of its mean position in January–February and south in August–September (Figure 6b). The seasonal near-coastal latitudinal shifts of the zero-transport contour are consistent with previous studies. For example, Strub and James (2002a) find most of the seasonal circulation variability in the northeast Pacific gyres to occur as strong residuals in the alongshore currents around the boundary of the basin, with maximum poleward Alaska Current in winter (December-February), at the same time that the equatorward California Current is at its weakest. In addition to the near-coastal seasonal changes in the bifurcation latitude, we also find that the Alaska Gyre fluctuates in size seasonally, expanding in winter and contracting in summer (Figure 6b). The annual shift in zero-meridional transport seen here follows the annual oscillation of the zero wind stress curl for the northeast Pacific (Pickart et al., 2009). This is consistent with a predominantly barotropic response at annual time scales of the Alaska Gyre circulation, governed by a time-dependent Sverdrup balance between meridional flow and wind stress curl (Qiu, 2002).

In addition to seasonal shifts, the zero-transport contour undergoes displacements on longer, interannual time scales, as much as ±2° latitude from its monthly mean position (Figure 6c). Some of the interannual variability is again confined closer to the coast (east of 140°W), implying changes in the alongshore currents. Most of the interannual variability, however, consists of multiyear latitudinal shifts of the zero transport

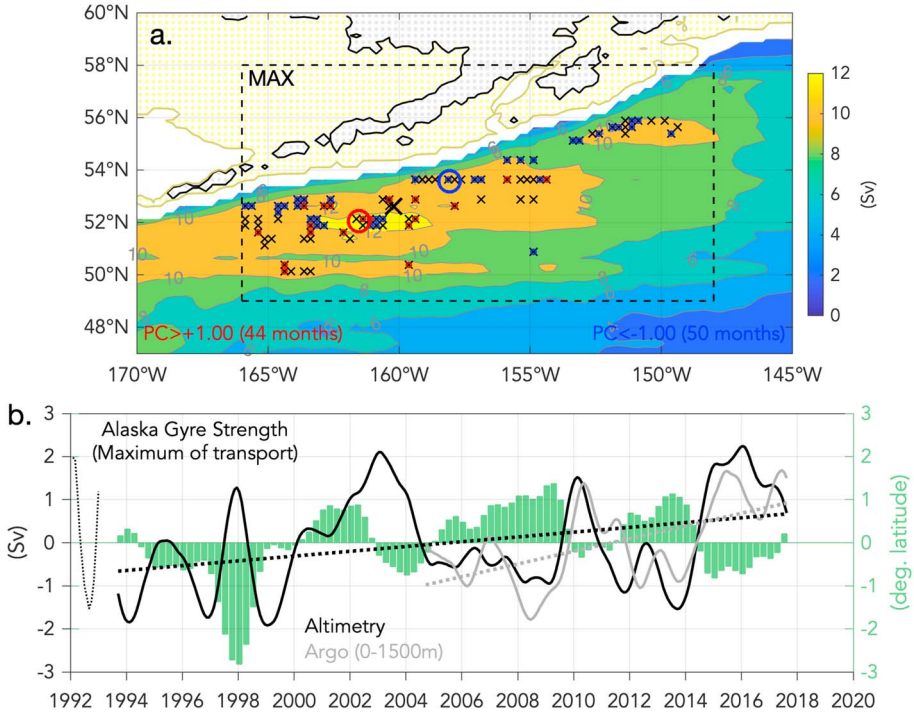

Figure 8. Interannual variability of the Alaska Gyre strength, determined from the maximum 0- to 1,500-m meridional transport (MAX box, also shown in Figure 3). (a) Map of the locations of transport maximum: monthly locations for the period 1993–2017 (black crosses), overlaid on the mean transport from altimetry (color shading). The maxima corresponding to a positive (negative) phase of the leading EOF (Figure 4d) are circled in red (blue), respectively, with the average maximum location during each phase shown with a larger circle. (b) Interannual variability of gyre strength from altimetry (in black), and from Argo 0–1,500 m (in gray). The linear trend over the corresponding data period is shown in matching color dotted line. Superimposed is the zero-transport latitude shift, averaged in 3-month intervals (green bars, axis on the right; same as Figure 7). The annual cycle of gyre strength (from altimetry) is plotted once starting in January 1992.

contour, nearly uniformly across the northeast Pacific region considered here, implying instead changes in the Alaska Gyre size.

Southward (negative) shifts of the zero-transport contour indicate a larger than average Alaska Gyre. Several such periods can be identified: 1997–1998, 2003–2004, 2010 (only a weak anomaly), and 2014–2016, with the largest southward shift (3° latitude from its mean position) occurring in the winter 1997/1998. Larger than average Alaska Gyre is associated with El Niño conditions over the tropical Pacific (Figure 6c; Multivariate ENSO Index [MEI] from https://www.esrl.noaa.gov/psd/enso/mei; Wolter & Timlin, 1998). Periods with La Niña conditions over the tropical Pacific are less common over the altimetric record. While El Niño years (especially strong El Niños) tend to be associated with larger than average Alaska Gyre, La Niña conditions do not necessarily mean contracted gyre; for example, 1999 and 2011 are both characterized with strong La Niña conditions, but there is no significant gyre-scale shift of the zero-transport contour (Figure 6c).

When averaged zonally across the northeast Pacific region, the time series of zero-transport latitude displacement from its mean position emphasizes the basin-scale variability of the bifurcation latitude (Figure 7). It can thus be interpreted as a measure of the Alaska Gyre size, with positive values (northward shift) indicating smaller Alaska Gyre. The low-frequency variability of gyre size since 1993 is punctuated by the four periods of larger than average Alaska Gyre (southward shift) during El Niño years as listed above, separated by periods of smaller than average Alaska Gyre (northward shift). There is no significant decadal trend in the size of the Alaska Gyre over the altimetric period, 1993–2017. Thus, the northward shift of the SSH contour separating the subtropical from Alaska Gyre noticed previously (Figure 2a) does not translate into a shrinking Alaska Gyre but is instead a reflection of the rising sea level over the last 25 years. The Alaska Gyre size tends to vary in opposite phase to the PDO index: A positive PDO phase is associated with a southward deflection and larger than average Alaska Gyre (Figure 7; $r = -0.56$, $p < 0.05$ for the zero-transport

latitude shift vs. PDO index). This is consistent with the variability captured by the leading EOF of meridional transport, which is strongly correlated with the PDO index and explains half of the transport variance (Figures 4c and 4d).

4.2. Strength of the Alaska Gyre

The maximum of the meridional geostrophic transport in the Alaska Gyre can be used as a measure of the strength of the gyre circulation. Examination of the sequence of daily meridional transport fields shows that on average the maximum transport occurs near 160°W, 52.5°N, but the location of the maximum can vary by as much as 8–10° zonally, as well as shift inshore and offshore (Figure 8a). Generally, during a positive phase of the leading transport EOF when the Alaska Gyre is stronger, its maximum is located farther west, while during a negative phase the maximum transports shifts east closer to the GOA (Figure 8a). Guided by the variability present in the data, we chose a box (named MAX in Figures 8a and 3), that encompasses the region where the maximum transport tends to occur.

With this definition, we find mean transport above 1,500 m for the Alaska Gyre of 14.2 Sv (from altimetry) and 13.0 Sv (based on Argo, integrated vertically 0–1,500 m). These numbers fall in line with other estimates of the Alaska Gyre intensity that put it in the 15- to 21-Sv range (Logan & Johnson, 2017; Reed, 1984; Stabeno & Hristova, 2014). Our Argo estimate is very close to the mean 0- to 1,500-m transport readily inferred from the depth-integrated steric height H from Cummins and Masson (2018). In their Figure 2, the difference in H across the Alaska Current at 52°N is ~150 m^2, giving a mean transport for the Alaska Gyre of $(g/f)\Delta H \approx$ 12.8 Sv.

The gyre strength fluctuates annually, with peak-to-peak amplitude of 3.5 Sv in altimetry and maximum in winter December–February (Figure 8b). The amplitude and phase of annual cycle are consistent with previous estimates (e.g., peak-to-peak amplitude of 2.8 Sv and a winter maximum in Qiu, 2002). Combined with the seasonal fluctuations in gyre size (Figure 7), this implies that the Alaska Gyre is stronger and expanded in winter while weaker and contracted in summer. The peak-to-peak amplitude of gyre transport annual cycle from Argo is much weaker (1.3 Sv). This is not surprising given that the ocean response to large-scale atmospheric forcing on annual and shorter time scales at high latitudes is expected to be mostly barotropic (Gill & Niiler, 1973) and thus captured by altimetry but not in Argo steric height. Specifically for the Alaska Gyre, it has been shown that seasonal variations in transport are largely governed by a time-dependent topographic Sverdrup balance (Qiu, 2002; Vivier et al., 1999).

The interannual variability in gyre strength is on the order of ±2 Sv, comparable to its annual cycle (Figure 8b). On interannual time scales, the altimetric and Argo time series agree quite well: The correlation coefficient between the two series is $r = 0.8$ ($p < 0.01$) for the common 2004–2017 period, with RMS magnitude of 1 Sv for both series during that period. This reaffirms that the linear fit applied to altimetry provides meaningful results for 0- to 1,500-m low-frequency transport variability. The interannual gyre strength variability is modestly anticorrelated with the bifurcation latitude shift ($r = -0.46$, $p < 0.10$), that is, the Alaska Gyre tends to be stronger when expanded and weaker when contracted. This is consistent with the pattern of circulation variability captured by the leading transport EOF for the northeast Pacific (Figures 4c and 4d). Generally, during a positive phase of the PDO, the Alaska Gyre tends to be stronger and larger. This PDO-correlated gyre strength modulation is reflected as well in the leading EOFs of isopycnal surfaces displacement over the Alaska Gyre down to a depth of at least 1,000 m (Cummins & Masson, 2018). As shown in their Figure 6, a positive phase of the PDO index and hence warmer SSTs over the region are associated with downward displacement of the pycnocline over the Alaska Gyre (based on the sigma 26.6 isopycnal), and results in strengthening of the gyre circulation.

In addition to the PDO-correlated interannual fluctuations, the Alaska Gyre strength shows a positive trend, present in both the altimetric and in the shorter Argo time series (Figure 8b). The difference in linear trend magnitude between Argo and altimetry reflects the different periods covered by the two data sets; if the altimetric trend is computed over the Argo period, the slopes are nearly identical. The trends are significant at 80% level (90% for Argo), assuming 18 (12) degrees of freedom, respectively (see section 2.2). Accumulated over the 25-year altimetric period, the trend implies that the Alaska Gyre is stronger now by about ~2 Sv compared to 1993, which is comparable to the magnitude of interannual and annual transport variations.

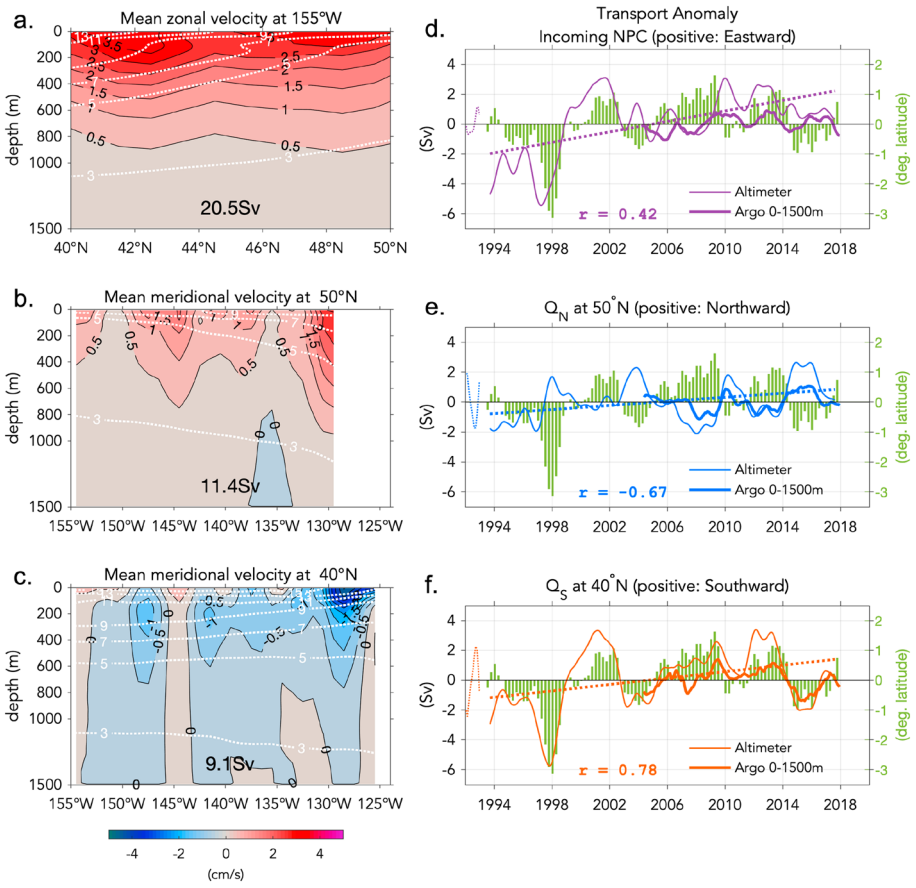

Figure 9. Split of transport at the bifurcation latitude (BI box in Figure 3). (a–c) Mean normal velocity (color shading; contour interval 0.5 cm/s) and temperature (white contours; contour interval 2 °C) from Argo on the (a) west (155°W), (b) north (50°N), and (c) south (40°N) side of the BI box. (d–f) Time series of corresponding transport (interannual anomaly) from Argo 0–1,500 m (thick line) and altimetry (thin line). The assumed direction of positive transport anomaly is indicated on each plot. The annual cycle of transport (from altimetry) is plotted once starting in January 1992. Overlaid is the zero-transport latitude shift, averaged in 3-month intervals (green bars, axis on the right; same as Figure 7). The correlation between transport anomaly (from altimetry) and zero-transport latitude shift is shown in each plot. NPC = North Pacific Current.

4.3. Transport Distribution at the Bifurcation Latitude

We seek to quantify the split of transport at the bifurcation streamline over the 25-year long altimetric record and establish its connection to the variability in Alaska Gyre size and strength. Previous studies, covering different and/or shorter time periods, suggest that shifts in the bifurcation latitude separating the subtropical from the Alaska Gyres are associated with variability in the transport distribution between the gyres (Cummins & Freeland, 2007; Douglass et al., 2006).

The northern and southern boundary for the bifurcation region examined here are chosen at 50°N and 40°N, respectively, with the zero-transport contour crossing diagonally through the region (box BI in Figure 3). The western edge of the BI box is at 155°W, ensuring that the bulk of the NPC transport deflected north into the GOA is accounted for. Mean velocity sections from Argo (referenced to 1,500 dbar) show predominantly northward velocity at 50°N, and southward velocity at 40°N (Figures 9a–9c). The Alaska Current at 50°N appears as boundary intensified current, while the California Current at 40°N is shifted slightly offshore. At the western side, the mean section consists of eastward zonal velocity through the water column, with isotherms sloping upward to the north.

Transport computed from the Argo velocities shows a closed mean mass balance for the BI region (Figures 9a–9c). The NPC between 40°N and 50°N brings in 20.5 Sv above 1,500 m, which are subsequently distributed, with 11.4 Sv (56%) flowing northward into the Alaska Gyre, and 9.1 Sv (44%) flowing southward into the subtropical gyre. In the discussion that follows, we will continue to use this "mass

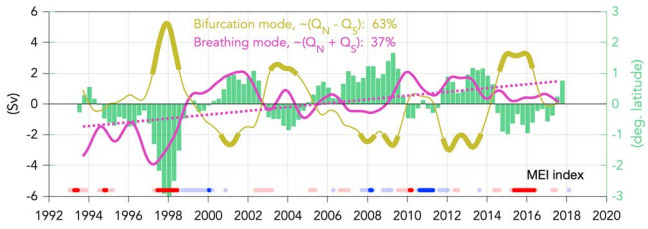

Figure 10. Northward Q_N and southward Q_S transport anomalies, split into bifurcation and breathing mode following Cummins and Freeland (2007). The bifurcation mode (representing mutually compensating Q_N and Q_S) accounts for 63% of the variance (yellow line), and is anticorrelated with the zero-transport latitude shift (green bars, axis on the right; same as Figure 7). Periods of strongly anticorrelated Q_N and Q_S anomalies (exceeding one standard deviation) are shown in thicker line. The breathing mode proportional to the total incoming transport anomaly $Q_N + Q_S$ (and representing positively correlated Q_N and Q_S) accounts for 37% of the variance and has a linear increasing trend (purple solid and dashed lines). Shown along the time axis is the MEI, with dark (light) red indicating strong (moderate) El Niño, and dark (light) blue, strong (moderate) La Niña conditions. MEI = Multivariate ENSO Index.

balance"-motivated sign convention for the split transports where both the northward transport Q_N, and southward transport Q_S, are positive when out of the bifurcation box. The slightly larger portion of NPC transport deflected northward is similar for the altimetry-estimated Q_N and Q_S and is consistent with findings from previous studies (e.g., Cummins & Freeland, 2007). Note, however, that the closed mass balance that we find here is somewhat fortuitous. A different choice of northern or southern boundary for the domain (with a lesser representation of the near-shore currents) could result in larger residuals and slightly different percentage of transport split. Consistent with previous studies (e.g., Strub & James, 2002a), we find only a weak seasonal cycle in the incoming NPC transport (peak-to-peak amplitude ~1 Sv), while the seasonal fluctuations are much larger (peak-to-peak amplitude of ~4 Sv) but mutually compensating for the northward and southward branches (Figures 9d–9f). The largest northward transport occurs in winter coinciding with the timing of largest and strongest Alaska Gyre (Figures 7 and 8), at the same time that the southward transport is at its weakest.

The distribution of transport at the bifurcation latitude varies significantly on interannual time scales (Figures 9d–9f). The magnitude of transport anomalies derived from altimetry tends to exceed the direct Argo estimates, due in part to the finer spatial resolution and better near-coastal coverage of the altimetric data (see Figure 1). Despite the difference in magnitude, the two estimates are highly correlated ($r = 0.87$, $p < 0.01$ for all three sections). On interannual time scales, Q_N and Q_S vary with the bifurcation latitude (Figures 9e and 9f). The northward transport Q_N is negatively correlated with the zero-transport contour shift ($r = -0.67$, $p < 0.01$), while the southward transport Q_S is positively correlated ($r = 0.78$, $p < 0.01$). Thus, when the bifurcation streamline shifts south (expanded Alaska Gyre), the transport northward across 50°N increases, while the transport southward across 40°N decreases. Additionally, both Q_N and Q_S show a positive trend (significant at 80%) over the 25-year altimetric record (but not over the shorter Argo period 2004–2017). In contrast to Q_N and Q_S, the incoming transport anomaly across the western boundary representative for the NPC is only modestly correlated to the bifurcation latitude shift (Figure 9d; $r = 0.42$, $p < 0.10$). Note that for the NPC, the altimetric time series is simply the sum of the northward and southward transport anomalies, so it is not an independent estimate.

The split of NPC transport in the northeast Pacific is often discussed in terms of its covarying and mutually compensating parts (Douglass et al., 2006) or using the so-called bifurcation and breathing modes (Cummins & Freeland, 2007). We refer to these modes here to put our results in the context of previous studies but also, since these modes clearly highlight the two types of variability seen in the altimetric data, long-term trend and bifurcation shift. Following Cummins and Freeland (2007), for two transport time series with zero mean, such as Q_N and Q_S, the bifurcation and breathing modes are an orthogonal decomposition of Q_N and Q_S that separates the positively from the negatively correlated variability in the two time series while preserving the total variance. The bifurcation mode, $Q_{Bi} = (Q_N - Q_S)/\sqrt{2}$, represents mutually compensating (negatively correlated) Q_N and Q_S anomalies for invariant total transport $Q_N + Q_S$, while the breathing mode, $Q_{Br} = (Q_N + Q_S)/\sqrt{2}$, represents instead changes in the total transport $Q_N + Q_S$ and positively correlated

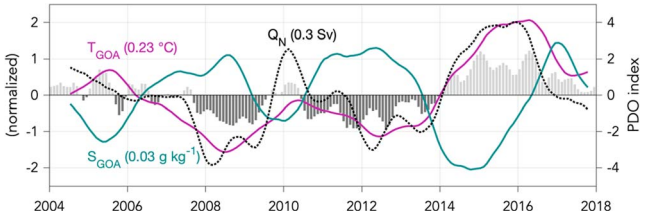

Figure 11. Interannual anomaly of top 300 m northward transport at 50°N (Q_N, black dotted line), and GOA volume-averaged above 300 m temperature (T_{GOA}, purple line) and salinity (S_{GOA}, blue line) from Argo (see GOA box in Figures 3 and 5 for the region definition). All three curves are scaled by their respective standard deviation (value indicated in parentheses). The PDO index is shown in gray shading (axis on the right). GOA = Gulf of Alaska; PDO = Pacific Decadal Oscillation.

Q_N and Q_S anomalies. When the two time series Q_N and Q_S are uncorrelated, the variance is split equally between the bifurcation and breathing modes.

Figure 10 shows the bifurcation and breathing modes computed based on the altimetric transport anomalies (Figures 9e and 9f). The Argo decomposition is similar in phase and sign but with smaller amplitude and is not shown here. During periods when Q_N and Q_S are anticorrelated the bifurcation mode is dominant. Amplitudes of the bifurcation mode exceeding ±1 standard deviation are emphasized with a thicker line, highlighting that the bifurcation mode is strongly anticorrelated with the shifts of the zero-transport contour ($r = -0.88$, $p < 0.01$). Combined with our previous findings about the Alaska Gyre strength and size (Figures 7 and 8), this clearly shows that a larger and stronger Alaska Gyre is associated with more transport northward, while smaller and weaker Alaska Gyre is associated with less transport northward. This variability is consistent with the leading PDO-correlated EOF accounting for more than half of the total transport variability (Figure 4). Consequently, and as expected, the bifurcation mode is also positively correlated with the PDO index ($r = 0.72$, $p < 0.01$).

The breathing mode on the other hand is proportional to variations in the total (incoming) transport Q_N+Q_S, and describes covarying changes in the northward and southward branch. It is only weakly correlated with the bifurcation latitude shift ($r = 0.43$, $p < 0.10$), and PDO index ($r = -0.47$, $p < 0.05$). In fact, most of this correlation is due to the sharp transport decrease and subsequent increase during the 1997/1998 El Niño and subsequent La Niña (Figure 10). Outside that period, the breathing mode is essentially uncorrelated with the bifurcation latitude shift ($r = 0.12$, $p = 0.70$ for 2004–2017). Instead, the breathing mode highlights the rising linear trend over the 25-year altimetric record, pointing to an increase in the NPC and as a consequence an increase in the transports deflected north into the Alaska Gyre and south into the subtropical gyre.

It is worth noting that using SSH differences for 1993–2005, Cummins and Freeland (2007) found that the breathing mode explains a larger fraction of the transport variance (breathing mode 65% versus bifurcation mode 35% of the total transport variance for 1993–2005). Here, we find instead that a larger fraction of the transport variance projects on the bifurcation mode (breathing mode 37% versus bifurcation mode 63% of the total transport variance for 1993–2017). The bifurcation mode captures the bulk of the total transport variance during the shorter Argo period as well (80% of the total variance for 2004–2017) for both the altimetric and Argo transport estimates, reflecting mostly the large mutually compensating anomalies for the California and Alaska Currents that occurred in 2015–2016 (Figures 9e and 9f). As noted in Cummins and Freeland (2007), the breathing and bifurcation modes are dominated by low frequencies, and thus it is not surprising that the fraction of variance in each mode varies depending on the period considered.

4.4. Geostrophic Contribution to Temperature and Salinity Variability in the GOA

We now consider the GOA region north of 50°N and east of 155°W, situated just north of the bifurcation box studied in the previous section (GOA box in Figure 3). As seen in section 4.3, the northward geostrophic transport across 50°N into the GOA covaries with the phase of the PDO. Temperature, T_{GOA}, and salinity, S_{GOA}, volume-averaged for the GOA and over the top 300 m of the water column, are also correlated with the PDO index (Figure 11). For the volume average and all calculations in this section, we consider only the top 300 m of the water column since temperature, salinity, and transport variability are dominated by upper layer changes, but the results are qualitatively similar for the top 1,500 m. During a positive phase of the PDO, the temperature in the GOA is warmer than average ($r = 0.85$, $p < 0.01$ for T_{GOA} versus PDO index), while salinity in the GOA is fresher than average ($r = -0.60$, $p < 0.05$ for S_{GOA} versus PDO index). The amplitude of interannual variability appears small: The RMS amplitude is 0.23 °C for T_{GOA} and 0.03 g/kg for S_{GOA}. These are, however, volume averages for the top 300 m and over a large spatial region; locally and near the surface changes in T and S are more substantial. The warmer and fresher T_{GOA} and S_{GOA} during a positive PDO phase are consistent with the expected water properties variations for the GOA associated with the PDO (Hermann et al., 2016; Cummins & Masson, 2018).

The covariability between northward transport and temperature and salinity anomalies for the GOA as a whole suggests a possible advective contribution where, for example, more warm waters are advected from the south into the GOA and contribute to its warming (in volume-averaged sense). We thus attempt to

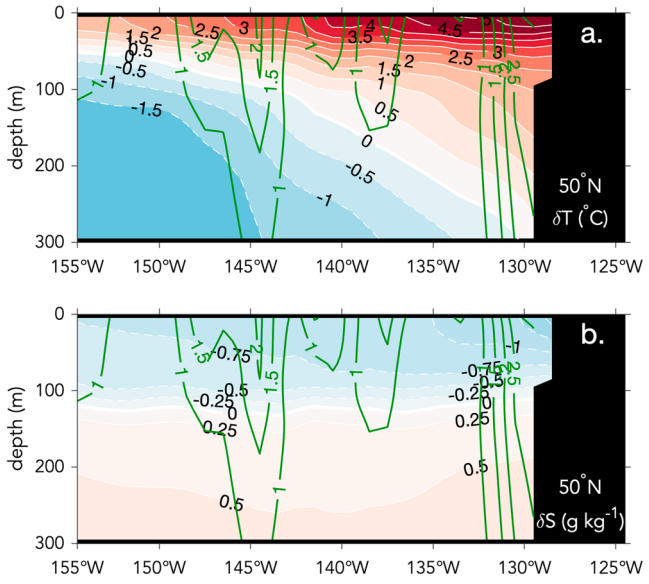

Figure 12. Mean 0- to 300-m section at 50°N from Argo of (a) anomalous temperature, δT, and (b) anomalous salinity, δS, where "anomalous" is defined as the departure from the volume average above 300 m for the GOA temperature and salinity, respectively. Overlaid in green are contours of mean meridional geostrophic velocity from Argo (contour interval 0.5 cm/s).

quantify the importance of the advective temperature and salinity fluxes across 50°N for the temperature and salinity variability in the GOA. For this analysis we rely on the Argo data set and derived meridional geostrophic velocity; the results are thus limited to the Argo period, 2004–2017 (for which there is no significant trend in the northward transport; see Figure 10). We focus solely on the 50°N section because of its physical relevance but also because the velocity there is reasonably well represented in the gridded Argo product (see Figures 9b and 9e). While it is pertinent to compare the results to the same analysis performed for the western boundary of the GOA region (section at 155°W; see Figure 3), the Argo-estimated zonal geostrophic velocity there is poorly resolved and any findings would be inconclusive. The discussion in this section is limited to the geostrophic contribution to advection of temperature and salinity; contribution due to Ekman transport has not been considered.

Computing a heat flux (or absolute temperature flux) in the presence of net mass transport, such as the section at 50°N, is ambiguous since the result is dependent on the zero-temperature reference (e.g., Freeland, 2002; Montgomery, 1974). However, Lee et al. (2004) introduce a more limited in scope calculation that can be done for any partial surface enclosing a control volume and without the requirement of closed mass balance, using the advection of anomalous temperature, where "anomalous" is defined as departure fromthe volume-averaged temperature for the control volume of interest. In the case of the GOA box and its south-bounding section at 50°N (Figure 3), this signifies that advection from the south would modify the temperature of the GOA if and only if it brings temperature different than the volume-averaged temperature for the GOA.

To illustrate the concept, Figure 12 shows the time mean meridional geostrophic velocity at 50°N, superimposed on the time mean temperature and salinity anomalies, δT and δS, computed with respect to the volume-averaged T_{GOA} and S_{GOA}, respectively. At 50°N, the temperature is warmer than the volume-averaged temperature T_{GOA} near the surface and close to the coast, while it is colder below 100 m and away from the coast (Figure 12a). Combined with the positive meridional velocity at 50°N (largest near the coast in the Alaska Current), this implies that the effect of geostrophic advection from the south on the top 300 m temperature in the GOA is positive; that is, geostrophic advection from the south warms the GOA, in the time mean. At 50°N, salinity is fresher than the volume-averaged salinity S_{GOA} above 100 m, and saltier below (Figure 12b), suggesting that geostrophic advection from the south decreases the top 300 m salinity GOA in the time mean.

What is of more interest here are the interannual variations of the advective temperature and salinity fluxes, which we denote by $\langle vT \rangle$ and $\langle vS \rangle$, and how they compare to the rate of change of temperature and salinity in the GOA box, $\frac{d}{dt} T_{GOA}$ and $\frac{d}{dt} S_{GOA}$. We obtain $\langle vT \rangle$ and $\langle vS \rangle$ by repeating for each month the calculation illustrated by Figure 12. That is, we compute the product of the monthly meridional geostrophic velocity v and monthly temperature and salinity anomalies, δT and δS, then integrate their product zonally and vertically across the 50°N section:

$$\langle vT \rangle = \left(\frac{1}{V_{GOA}} \int_0^{300\,m} \int_{50°N} dz\,dx (v\delta T) \right)', \quad (2)$$

$$\langle vS \rangle = \left(\frac{1}{V_{GOA}} \int_0^{300\,m} \int_{50°N} dz\,dx (v\delta S) \right)'. \quad (3)$$

Here, V_{GOA} is the volume of the GOA region (box GOA in Figure 3, above 300 m), while δT and δS are the temperature and salinity anomalies with respect to the volume-averaged T_{GOA} and S_{GOA} for that month (for reference, Figure 11 shows the monthly time series of T_{GOA} and S_{GOA}, but with the mean and annual cycle removed). We obtain the interannual anomalies for the advective fluxes, $\langle vT \rangle$ and $\langle vS \rangle$, by removing the mean

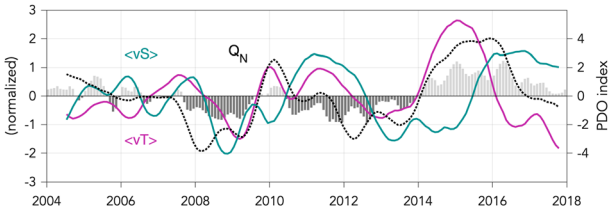

Figure 13. Interannual anomaly of 0- to 300-m geostrophic advective flux at 50°N for temperature ($\langle vT \rangle$, purple line), salinity ($\langle vS \rangle$, blue line), and northward transport (Q_N, black dotted line). All three curves are scaled by their respective standard deviation (see Figure 14 for the magnitude of $\langle vT \rangle$ and $\langle vS \rangle$). The PDO index is shown in gray shading (axis on the right). PDO = Pacific Decadal Oscillation.

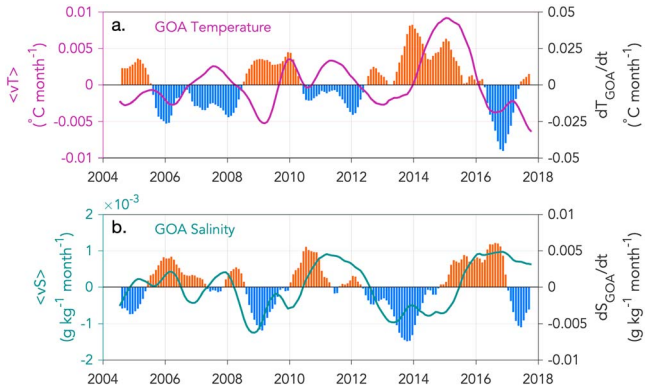

Figure 14. (a) Interannual anomaly of geostrophic temperature flux $\langle vT \rangle$ at 50°N (purple line, axis on the left) and rate of change of temperature in the GOA box, dT_{GOA}/dt (red/blue shading, axis on the right). (b) Interannual anomaly of geostrophic salinity flux $\langle vS \rangle$ at 50°N (blue line, axis on the left) and rate of change of salinity in the GOA box, dS_{GOA}/dt (red/blue shading, axis on the right). The rate of change of T_{GOA} and S_{GOA} are the time derivatives of the volume-averaged T_{GOA} and S_{GOA} shown in Figure 11. GOA = Gulf of Alaska.

and annual cycle and smoothing with a 7-month running mean (operation marked by prime).

Geostrophic advection of temperature from the south is positively correlated with the northward transport anomaly Q_N ($r = 0.55$, $p < 0.05$; Figure 13). During periods of larger northward transport, advective temperature flux from the south acts to warm the GOA. However, comparing the magnitudes of the rate of change of temperature in the GOA, dT_{GOA}/dt, and the geostrophic advective contribution, $\langle vT \rangle$, shows that the advective flux is a factor of 5 smaller in magnitude (Figure 14a). Additionally, it is only during 2015–2016, associated with the marine heat wave event in the northeast Pacific (the "Blob"; Bond et al., 2015; Di Lorenzo & Mantua, 2016) that the temperature advective flux acts in the right direction, that is, contributing to the warming and subsequent cooling of the GOA. For the years prior to that, including the beginning of the Blob in 2013–2014, the sign of $\langle vT \rangle$ is mostly unrelated to that of dT_{GOA}/dt and often acts in the opposite direction. This suggests that although on occasion geostrophic advection from the south can contribute to the warming and cooling of the GOA, in general it does not play a major role for the interannual temperature anomalies in the GOA, and other (local) processes are more important.

Geostrophic advection of salinity is also positively correlated with the northward transport anomaly Q_N (Figure 13). However, the correlation is largest with a 12-month lag ($r = 0.80$, $p < 0.01$). In general, the interannual variations of an advective flux, such as $\langle vS \rangle$, are due to a combination of anomalous advection of mean salinity and mean advection of anomalous salinity, so proportionality between Q_N and $\langle vS \rangle$ is not required. The lag between Q_N and $\langle vS \rangle$ indicates that the mean and anomalous salinity and velocity at the 50°N section combine in such a way that the largest salinity advective flux occurs a year after the largest transport anomalies. Similar to the case of temperature, geostrophic advection of salinity is a factor of 5 smaller when compared to the rate of change of S_{GOA} (Figure 14b). However, unlike for $\langle vT \rangle$ the timing of positive and negative contributions from $\langle vS \rangle$ matches much closer the actual periods of increasing or decreasing S_{GOA}. This suggests that geostrophic advection of salinity from the south contributes to the salinity anomalies in the GOA; however, it is not the dominant factor, with local processes and surface fluxes playing a much more important role.

5. Summary

We examined the variability of the large-scale Alaska Gyre circulation over a 25-year period (1993–2017), based on the top 1,500 m meridional geostrophic transport derived from Argo and altimetry (section 3.3). Two different types of modes characterize the low-frequency variability of Alaska Gyre circulation: PDO-related fluctuations in gyre strength and areal extent, and a long-term trend affecting the gyre strength as well as northward transport into the GOA.

More than half of the meridional transport variance for the northeast Pacific projects on a statistical mode that is consistent with the PDO-mode of SST variability for the North Pacific (Di Lorenzo et al., 2013; Mantua et al., 1997; Figure 4). During a positive phase of the PDO, the zero-transport streamline separating the subtropical from the Alaska Gyre is shifted to the south from its mean position, while more transport is diverted northward, associated with a stronger and expanded Alaska Gyre (Figures 6 and 8). This translates into mutually compensating northward and southward transport anomalies, strongly correlated with the position of the zero-transport contour. We find that this PDO-correlated mode of variability (also called bifurcation mode in Cummins & Freeland, 2007) accounts for 63% of the transport variance over the altimetric period 1993–2017 (Figure 10).

Additionally, over the 25-year altimetric record there is a linear, increasing trend in the strength of the Alaska Gyre, accompanied by an increasing trend of the incoming, eastward flowing NPC (Figures 8 and 9). In-phase (positively correlated) anomalies of the incoming NPC and northward and southward anomalies at the bifurcation latitude account for the remaining 37% of transport variance (called also breathing mode in Cummins & Freeland, 2007; Figure 10). Despite the northward shifting SSH contours over the altimetric

1993–2017 record (due to sea level rise; Figure 2), we do not find a trend in the areal extent of the Alaska Gyre during that period, based on the shifts of the zero-transport contour separating northward from southward flow (Figure 7).

Temperature and salinity, volume-averaged for the GOA and the top 300 m, are also strongly affected by the PDO, with warmer and fresher waters during a positive phase (Cummins & Masson, 2018; Hermann et al., 2016). The covariability between northward geostrophic transport anomalies and water property variability in the GOA suggest a possible advective contribution from the south (Figure 11). However, comparison between the magnitudes of temperature and salinity advective fluxes across 50°N and the rate of change of temperature and salinity in the GOA shows that geostrophic advection plays only a secondary role (Figure 14). For temperature in particular, it is only in the aftermath of the ocean heat wave of 2013/2014 (Bond et al., 2015) that advective flux from the south played a more appreciable role for the warming and subsequent cooling of the GOA. Analysis of the large-scale Argo density field in the northeast Pacific by Cummins and Masson (2018) similarly suggests that large spice anomalies in the GOA appear to be produced locally in the northeast Pacific, instead of advected from the west, limiting the potential for decadal prediction of upper ocean conditions over the region.

The analysis presented here focused on the large-scale, interannual-to-decadal variability and trends of the circulation and physical conditions in the GOA, providing a historical context for the effect of global climate modes on the region. Ultimately, variability of the large-scale circulation is but one of the factors influencing the complex ecosystem found in the GOA (Royer & Grosch, 2006; Stabeno et al., 2016).

Acknowledgments
This is contribution number 18-397 from the Joint Institute for Marine and Atmospheric Research, contribution number 4937 from NOAA/Pacific Marine Environmental Laboratory, and contribution EcoFOCI-0925 to NOAA's Ecosystems and Fisheries-Oceanography Coordinated Investigations. The Ssalto/Duacs altimeter products were produced and distributed by the Copernicus Marine and Environment Monitoring Service (http://www.marine.copernicus.eu). The 1992–2012 mean ocean dynamic topography data of Maximenko et al. (2009) are available online (http://apdrc.soest.hawaii.edu/projects/DOT). Argo data were collected and made freely available by the International Argo Program and the national programs that contribute to it (http://www.argo.ucsd.edu, http://argo.jcommops.org). The Argo Program is part of the Global Ocean Observing System (Argo, 2000). The Roemmich-Gilson Argo Climatology can be obtained online (http://sio-argo.ucsd.edu/RG_Climatology.html).

References

Argo (2000). Argo float data and metadata from Global Data Assembly Centre (Argo GDAC). *SEANOE*. https://doi.org/10.17882/42182

Bond, N. A., Cronin, M. F., Freeland, H. J., & Mantua, N. (2015). Causes and impacts of the 2014 warm anomaly in the NE Pacific. *Geophysical Research Letters*, *42*, 3414–3420. https://doi.org/10.1002/2015GL063306

Cazenave, A., Palanisamy, H., & Ablain, M. (2018). Contemporary sea level changes from satellite altimetry: What have we learned? What are the new challenges? *Advances in Space Research*, *62*, 1639–1653. https://doi.org/10.1016/j.asr.2018.07.017

Cazenave, A., & Remy, F. (2011). Sea level and climate: Measurements and causes of changes. *Wires Climate Change*, *2*(5), 647–662. https://doi.org/10.1002/wcc.139

Chelton, D. B., & Davis, R. E. (1982). Monthly mean sea-level variability along the west coast of North America. *Journal of Physical Oceanography*, *12*(8), 757–784. https://doi.org/10.1175/1520-0485(1982)012<0757:MMSLVA>2.0.CO;2

Crawford, W. R. (2002). Physical characteristics of Haida eddies. *Journal of Oceanography*, *58*, 703–713. https://doi.org/10.1023/A:1022898424333

Cummins, P. F., & Freeland, H. J. (2007). Variability of the North Pacific Current and its bifurcation. *Progress in Oceanography*, *75*(2), 253–265. https://doi.org/10.1016/j.pocean.2007.08.006

Cummins, P. F., & Lagerloef, G. S. E. (2004). Wind-driven interannual variability over the northeast Pacific Ocean. *Deep-Sea Research Part I*, *51*(12), 2105–2121. https://doi.org/10.1016/j.dsr.2004.08.004

Cummins, P. F., Lagerloef, G. S. E., & Mitchum, G. (2005). A regional index of northeast Pacific variability based on satellite altimeter data. *Geophysical Research Letters*, *32*, L17607. https://doi.org/10.1029/2005GL023642

Cummins, P. F., & Masson, D. (2018). Low-frequency isopycnal variability in the Alaska Gyre from Argo. *Progress in Oceanography*, *168*, 310–324. https://doi.org/10.1016/j.pocean.2018.09.014

Di Lorenzo, E., Combes, V., Keister, J. E., Strub, P. T., Thomas, A. C., Franks, P. J. S., et al. (2013). Synthesis of Pacific Ocean climate and ecosystem dynamics. *Oceanography*, *26*(4), 68–81. https://doi.org/10.5670/oceanog.2013.76

Di Lorenzo, E., & Mantua, N. (2016). Multi-year persistence of the 2014/15 North Pacific marine heatwave. *Nature Climate Change*, *6*, 1042–1047. https://doi.org/10.1038/nclimate3082

Di Lorenzo, E., Schneider, N., Cobb, K. M., Franks, P. J. S., Chhak, K., Miller, A. J., et al. (2008). North Pacific Gyre Oscillation links ocean climate and ecosystem change. *Geophysical Research Letters*, *35*, L08607. https://doi.org/10.1029/2007GL032838

Douglass, E., Roemmich, D., & Stammer, D. (2006). Interannual variability in northeast Pacific circulation. *Journal of Geophysical Research*, *111*, C04001. https://doi.org/10.1029/2005jc003015

Freeland, H. J. (2002). The heat flux across line-P 1996–1999. *Atmosphere Ocean*, *40*(1), 81–89. https://doi.org/10.3137/ao.400105

Freeland, H. J. (2006). What proportion of the North Pacific Current finds its way into the Gulf of Alaska? *Atmosphere Ocean*, *44*(4), 321–330. https://doi.org/10.3137/ao.440401

Gill, A. E., & Niiler, P. P. (1973). The theory of the seasonal variability in the ocean. *Deep-Sea Research*, *20*(2), 141–177. https://doi.org/10.1016/0011-7471(73)90049-1

Hermann, A. J., Ladd, C., Cheng, W., Curchitser, E. N., & Hedstrom, K. (2016). A model-based examination of multivariate physical modes in the Gulf of Alaska. *Deep-Sea Research Part II*, *132*, 68–89. https://doi.org/10.1016/j.dsr2.2016.04.005

IOC, SCOR, & IAPSO (2010). The international thermodynamic equation of seawater—2010: Calculation and use of thermodynamic properties (Tech. Rep. No. 56): Intergovernmental Oceanographic Commission, Manuals and Guides, UNESCO (English). Retrieved from http://www.TEOS-10.org

Ladd, C., Crawford, W. R., Harpold, C. E., Johnson, W. K., Kachel, N. B., Stabeno, P. J., & Whitney, F. (2009). A synoptic survey of young mesoscale eddies in the eastern Gulf of Alaska. *Deep-Sea Research Part II*, *56*(24), 2460–2473. https://doi.org/10.1016/j.dsr2.2009.02.007

Ladd, C., Kachel, N. B., Mordy, C. W., & Stabeno, P. J. (2005). Observations from a Yakutat eddy in the northern Gulf of Alaska. *Journal of Geophysical Research*, *110*, C03003. https://doi.org/10.1029/2004JC002710

Ladd, C., Stabeno, P. J., & Cokelet, E. D. (2005). A note on cross-shelf exchange in the northern Gulf of Alaska. *Deep-Sea Research Part II*, *52*(5–6), 667–679. https://doi.org/10.1016/j.dsr2.2004.12.022

Lee, T., Fukumori, I., & Tang, B. (2004). Temperature advection: Internal versus external processes. *Journal of Physical Oceanography*, *34*(8), 1936–1944. https://doi.org/10.1175/1520-0485(2004)034<1936:TAIVEP>2.0.CO;2

Logan, P. D., & Johnson, G. C. (2017). Zonal evolution of Alaskan Stream structure and transport quantified with Argo data. *Journal of Geophysical Research: Oceans*, *122*, 821–833. https://doi.org/10.1002/2016JC012302

Mantua, N. J., Hare, S. R., Zhang, Y., Wallace, J. M., & Francis, R. C. (1997). A Pacific interdecadal climate oscillation with impacts on salmon production. *Bulletin of the American Meteorological Society*, *78*(6), 1069–1080. https://doi.org/10.1175/1520-0477(1997)078<1069:APICOW>2.0.CO;2

Maximenko, N., Niiler, P., Centurioni, L., Rio, M.-H., Melnichenko, O., Chambers, D., et al. (2009). Mean dynamic topography of the ocean derived from satellite and drifting buoy data using three different techniques. *Journal of Atmospheric and Oceanic Technology*, *26*(9), 1910–1919.

McDougall, T. J., & Barker, P. M. (2011). Getting started with TEOS-10 and the Gibbs seawater(GSW) oceanographic toolbox. SCOR/IAPSO WG127.

Montgomery, R. B. (1974). Comments on "Seasonal variability of the Florida Current", by Niiler and Richardson. *Journal of Marine Research*, *32*, 533–35.

Mordy, C. W., Stabeno, P. J., Kachel, N. B., Kachel, D., Ladd, C., Zimmerman, M., et al. (2019). Patterns of flow in the canyons of the northern Gulf of Alaska. *Deep Sea Research Part II*. https://doi.org/10.1016/j.dsr2.2019.03.009

Pickart, R. S., Macdonald, A. M., Moore, G. W. K., Renfrew, I. A., Walsh, J. E., & Kessler, W. S. (2009). Seasonal evolution of Aleutian low pressure systems: Implications for the North Pacific subpolar circulation. *Journal of Physical Oceanography*, *39*(6), 1317–1339. https://doi.org/10.1175/2008JPO3891.1

Qiu, B. (2002). Large-scale variability in the midlatitude subtropical and subpolar North Pacific Ocean: Observations and causes. *Journal of Physical Oceanography*, *32*(1), 353–375. https://doi.org/10.1175/1520-0485(2002)032<0353:LSVITM>2.0.CO;2

Qiu, B., Schneider, N., & Chen, S. (2007). Coupled decadal variability in the North Pacific: An observationally constrained idealized model. *Journal of Climate*, *20*(14), 3602–3620. https://doi.org/10.1175/JCLI4190.1

Reed, R. K. (1984). Flow of the Alaskan Stream and its variations. *Deep-Sea Research Part*, *31*(4), 369–386. https://doi.org/10.1016/0198-0149(84)90090-6

Reed, R. K., & Stabeno, P. J. (1989). Recent observations of variability in the path and vertical structure of the Alaskan Stream. *Journal of Physical Oceanography*, *19*(10), 1634–1642. https://doi.org/10.1175/1520-0485(1989)019<1634:ROOVIT>2.0.CO;2

Reed, R. K., & Stabeno, P. J. (1993). The recent return of the Alaskan Stream to Near Strait. *Journal of Marine Research*, *51*(3), 515–527. https://doi.org/10.1357/0022240933224025

Roemmich, D., & Gilson, J. (2009). The 2004-2008 mean and annual cycle of temperature, salinity, and steric height in the global ocean from the Argo Program. *Progress in Oceanography*, *82*(2), 81–100. https://doi.org/10.1016/j.pocean.2009.03.004

Royer, T. C., & Grosch, C. E. (2006). Ocean warming and freshening in the northern Gulf of Alaska. *Geophysical Research Letters*, *33*, L16605. https://doi.org/10.1029/2006GL026767

Stabeno, P. J., Bell, S., Cheng, W., Danielson, S., Kachel, N. B., & Mordy, C. W. (2016). Long-term observations of Alaska Coastal Current in the northern Gulf of Alaska. *Deep-Sea Research Part II*, *132*, 24–40. https://doi.org/10.1016/j.dsr2.2015.12.016

Stabeno, P. J., Bond, N. A., Hermann, A. J., Kachel, N. B., Mordy, C. W., & Overland, J. E. (2004). Meteorology and oceanography of the northern Gulf of Alaska. *Continental Shelf Research*, *24*(7–8), 859–897. https://doi.org/10.1016/j.csr.2004.02.007

Stabeno, P. J., & Hristova, H. G. (2014). Observations of the Alaskan Stream near Samalga Pass and its connection to the Bering Sea: 2001–2004. *Deep-Sea Research Part I*, *88*(06), 30–46. https://doi.org/10.1016/j.dsr.2014.03.002

Strub, P. T., & James, C. (2002a). Altimeter-derived surface circulation in the large-scale NE Pacific Gyres. Part 1: Seasonal variability. *Progress in Oceanography*, *53*(2–4), 163–183. https://doi.org/10.1016/S0079-6611(02)00029-0

Strub, P. T., & James, C. (2002b). Altimeter-derived surface circulation in the large-scale NE Pacific Gyres. Part 2: 1997–1998 El Niño anomalies. *Progress in Oceanography*, *53*(2–4), 185–214. https://doi.org/10.1016/S0079-6611(02)00030-7

Tabata, S. (1982). The anticyclonic, baroclinic eddy off Sitka, Alaska, in the northeast Pacific Ocean. *Journal of Physical Oceanography*, *12*(11), 1260–1282. https://doi.org/10.1175/1520-0485(1982)012<1260:TABEOS>2.0.CO;2

Vivier, F., Kelly, K. A., & Thompson, L. (1999). Contributions of wind forcing, waves, and surface heating to sea surface height observations in the Pacific Ocean. *Journal of Geophysical Research*, *104*(C9), 20,767–20,788. https://doi.org/10.1029/1999JC900096

Wolter, K., & Timlin, M. S. (1998). Measuring the strength of ENSO events—How does 1997/98 rank? *Weather*, *53*, 315–324. https://doi.org/10.1002/j.1477-8696.1998.tb06408.x